

# SCIENTIFIC REPORTS



OPEN

## Enhanced thermoelectric performance of a chalcopyrite compound $\text{CuIn}_3\text{Se}_{5-x}\text{Te}_x$ ( $x = 0\sim 0.5$ ) through crystal structure engineering

Received: 27 September 2016

Accepted: 01 December 2016

Published: 06 January 2017

Yufu Lu<sup>1,2</sup>, Shaoping Chen<sup>1</sup>, Wenchang Wu<sup>2</sup>, Zhengliang Du<sup>2</sup>, Yimin Chao<sup>3</sup> & Jiaolin Cui<sup>2</sup>

In this work the chalcopyrite  $\text{CuIn}_3\text{Se}_{5-x}\text{Te}_x$  ( $x = 0\sim 0.5$ ) with space group  $I\bar{4}2m$  through isoelectronic substitution of Te for Se have been prepared, and the crystal structure dilation has been observed with increasing Te content. This substitution allows the anion position displacement  $\Delta u = 0.25 - u$  to be zero at  $x \approx 0.15$ . However, the material at  $x = 0.1$  ( $\Delta u = 0.15 \times 10^{-3}$ ), which is the critical Te content, presents the best thermoelectric (TE) performance with dimensionless figure of merit  $ZT = 0.4$  at 930 K. As  $x$  value increases from 0.1, the quality factor  $B$ , which informs about how large a  $ZT$  can be expected for any given material, decreases, and the TE performance degrades gradually due to the reduction in  $n_H$  and enhancement in  $\kappa_L$ . Combining with the  $ZT$ s from several chalcopyrite compounds, it is believable that the best thermoelectric performance can be achieved at a certain  $\Delta u$  value ( $\Delta u \neq 0$ ) for a specific space group if their crystal structures can be engineered.

Thermoelectric (TE) materials have their potential applications in power generation and cooling systems, therefore, they have received great attention in recent decades. The TE performance of the materials is characterized by the dimensionless figure of merit ( $ZT$ ),  $ZT = T\alpha^2\sigma/\kappa = T\alpha^2\sigma/(\kappa_L + \kappa_e)$ , here  $T$  is the absolute temperature, and  $\alpha$ ,  $\sigma$ ,  $\kappa$ ,  $\kappa_L$  and  $\kappa_e$  are the Seebeck coefficient, electrical conductivity, total thermal conductivity, lattice contribution and electronic part respectively. However, it is difficult to be improved as the  $\alpha$ ,  $\sigma$  and  $\kappa_e$  are usually coupled with each other strongly, which makes an independent property manipulation challenging for enhancing  $ZT$ .

In order to significantly improve the TE performance or  $ZT$  value, it is strongly necessary to explore effective strategies, in addition to those like nanostructure engineering<sup>1-3</sup> and band structure engineering<sup>4-6</sup>. Under the guidance of such strategies, many new materials with high TE performance have been developed. The typical materials are those with high crystal symmetry structure like  $\text{PbTe}$ <sup>4-6</sup>,  $\text{SnSe}$ <sup>7,8</sup>,  $\text{Mg}_2\text{Si}_{1-x}\text{Sn}_x$  solid solutions<sup>9,10</sup>, and half-Heusler (HH) alloys<sup>11</sup>.

Beyond those solid solutions, non-cubic diamond-like compounds, such as  $\text{CuGa(In)Te}_2$ ,  $\text{ZnSnP}_2$  and  $\text{Cu}_2\text{ZnSnS}_4$ , have also high power factors and  $ZT$ s if band convergence can be realized<sup>12,13</sup>. The band converges only when the tetragonal deformation parameter  $\eta$  ( $\eta = c/2a$ , where  $c$  and  $a$  are the lattice parameters) becomes unity or the crystal field splitting  $\Delta_{\text{CF}}$  approaches zero. However, deep investigations have revealed that as  $\eta$  approaches unity the chalcopyrite compounds often give low electrical conductivity and carrier concentration, due to the electrical inactivity caused by the attractive interaction between intrinsic donor-acceptor defect pairs<sup>14-16</sup>. In addition, the cation-anion bond lengths in many chalcopyrite compounds are around 0.26–0.28 nm<sup>17,18</sup>, a tiny disturbance of periodical crystal structure could have a profound impact on the phonon scattering mechanism. When  $\eta = 1$  ( $\Delta_{\text{CF}} = 0$ ) non-cubic diamond-like compounds become pseudocubic ones<sup>12,13</sup>. In this case, the least lattice distortion can be obtained and phonon scattering in point defect gets the minimum. As a result, the highest lattice part  $\kappa_L$  can be attained<sup>19</sup>.

<sup>1</sup>Materials Science and Engineering College, Taiyuan University of Technology, Taiyuan, 030024, China. <sup>2</sup>School of Materials & Chemical Engineering, Ningbo University of Technology, Ningbo, 315016, China. <sup>3</sup>School of Chemistry, University of East Anglia, Norwich NR4 7TJ, United Kingdom. Correspondence and requests for materials should be addressed to S.C. (email: [sxchenshaoping@163.com](mailto:sxchenshaoping@163.com)) or Y.C. (email: [Y.Chao@uea.ac.uk](mailto:Y.Chao@uea.ac.uk)) or J.C. (email: [cuijl@nbut.edu.cn](mailto:cuijl@nbut.edu.cn))

The aforementioned different findings suggest that the impact of crystal structure on TE performance seems to be much more complex than what we anticipated. The origin might be the presence of different space groups for each compound caused by the vacancy that exists in some chalcopyrites with different site assignments<sup>20</sup>. For example, in CuIn<sub>3</sub>Se<sub>5</sub> the sum of cation atoms is less than that of anion atoms, therefore, the structure formula of CuIn<sub>3</sub>Se<sub>5</sub> per unit cell is represented by Cu<sub>1.6</sub>In<sub>4.8</sub>□<sub>1.6</sub>Se<sub>8</sub> where □ denotes structure vacancy<sup>20</sup>. Therefore, the candidate space groups for CuIn<sub>3</sub>Se<sub>5</sub> can be  $I\bar{4}$ ,  $I4m2$ ,  $I\bar{4}2m$ ,  $I\bar{4}c2$ <sup>20</sup>. Since different space group gives different chemical bonding, which gives rise to different physical properties, it is strongly necessary to tune the TE performance through engineering the crystal structure.

Although CuIn<sub>3</sub>Se<sub>5</sub> have several space groups, the previous investigations have revealed that it still is a compound with defect non-cubic chalcopyrite structure<sup>21–26</sup> with  $\eta = 0.997 \sim 1.013$ <sup>27,28</sup>. Therefore, it is possible to engineer its crystal structure through manipulating its chemical compositions without changing its chalcopyrite structure. The tetragonal deformation parameter  $\eta$  is directly related to the anion position displacement  $u$  in chalcopyrites  $I_{(m-3)}III_{(m+1)}VI_{2m}$ , here  $m = 4, 5, 6, 7, 8, 9 \dots$ ; I = Cu, Ag; III = Al, Ga, In; VI = Te, Se, S<sup>29–31</sup>,  $u$  (or  $\Delta u = 0.25 - u$ ) tends to be 0.25 (or zero) as  $\eta$  approaches unity<sup>31</sup>. In addition, the anion position displacement  $u$  in CuIn<sub>3</sub>Se<sub>5</sub> fluctuates around 0.2435–0.2515<sup>27,28</sup>, which facilitates us to examine the  $\Delta u$  related TE performance as  $\Delta u$  is around zero.

In this work, the CuIn<sub>3</sub>Se<sub>5</sub>-based compounds have been prepared, and their crystal structures through isoelectronic substitution of Te with lower electronegativity (2.1) for Se (2.55) have been engineered. It is believable that such an isoelectronic substitution is very important, because it tends to elongate the bond lengths  $d_{\text{Cu-Te}}$  and  $d_{\text{In-Te}}$  due to an increased repulsion between Cu- or In-Te bonds. Therefore, it has potential to manipulate the  $\Delta u$  value, and optimize their TE performance.

## Experimental

**Sample preparations.** Four elements Cu, In, Te and Se with a purity of 99.999% were loaded into different silica tubes in vacuum according to the formula CuIn<sub>3</sub>Se<sub>5-x</sub>Te<sub>x</sub> ( $x = 0, 0.05, 0.1, 0.2, 0.5$ ), and then melted at 1273 K for 24 h, followed by a rapid cooling to RT in water. The as-solidified ingots were pulverized and then ball milled in stainless steel bowls containing benzinum at a rotation rate of 350 rpm for 5 h. The dried powders were sintered using spark plasma sintering apparatus (SPS-1030) under a pressure of 60 MPa and at the highest temperature of ~950 K. The total sintering time is about 5 min. The densities ( $d$ ) of the sintered samples ( $5.43 \sim 5.48 \times 10^3 \text{ kg/m}^3$ ), which are more than 95% theoretical values<sup>24</sup>, were measured using Archimedes' method. The sintered block with the sizes of  $\phi 20 \text{ mm} \times 3.0 \text{ mm}$  was cut into 3 mm-wide slices measuring  $2.5 \text{ mm} \times 12 \text{ mm}$  for electrical property measurement, and that with  $\phi \sim 10.0 \text{ mm} \times 2.0 \text{ mm}$  was obtained for thermal diffusivity measurement.

**Structural analyses.** The structural analysis of the powders was made by powder X-ray diffractometer (D8 Advance) operating at 50 kV and 40 mA. Cu K $\alpha$  radiation ( $\lambda = 0.15406 \text{ nm}$ ) and a scan rate of  $4^\circ \text{ min}^{-1}$  were used to record the patterns in the range from  $10^\circ$  to  $140^\circ$ .

In order to gain a deep understanding of the crystal structure, the microstructures of the samples ( $x = 0, 0.1$ ) have been examined by using high resolution transmission electron microscopy (HRTEM), and pure CuIn<sub>3</sub>Se<sub>5</sub> was examined for comparison. HRTEM images were obtained at 220 kV using JEM-2010F (Field emission TEM).

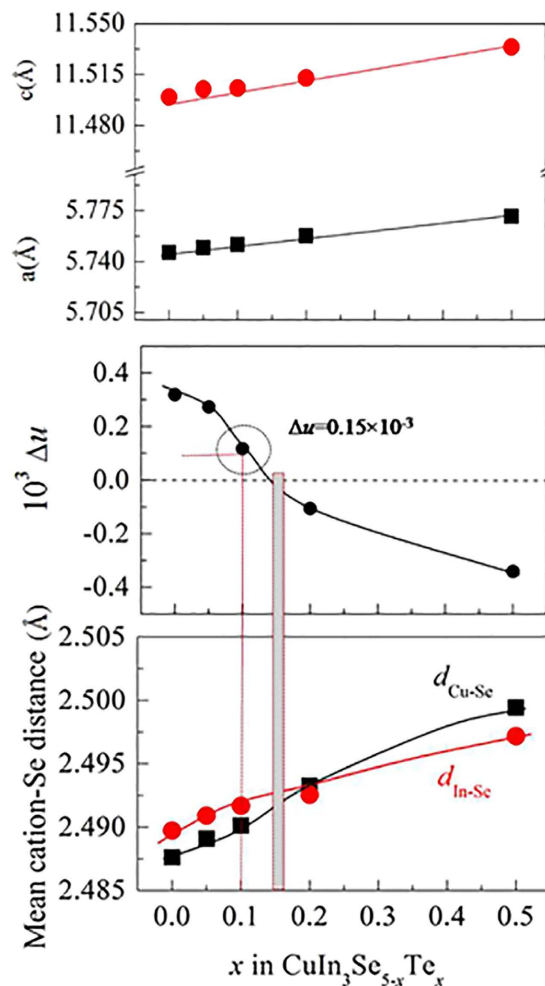
**TE transport property measurements.** The Hall coefficient ( $R_H$ ) measurements at room temperature (RT) were conducted on a Physical Property Measurement System (PPMS, Model-9) using a four probe configuration with a magnetic field sweeping between  $\pm 2.0 \text{ T}$ , and were performed on rectangular samples with size  $2 \times 2 \times 7 \text{ mm}^3$ . The Hall carrier concentrations ( $n_H$ ) and mobility  $\mu$  were subsequently calculated based on the following formulae  $n_H = -1/(e|R_H|)$ ,  $\mu = |R_H|\sigma$ , where  $e$  is the electron charge. The electrodes were fine copper wires for current and Hall voltage measurements, and the contacts were made of silver paste.

The Seebeck coefficients ( $\alpha$ ) and electrical conductivities ( $\sigma$ ) were measured as a function of temperature using ULVAC ZEM-3 instrument under helium atmosphere from RT to ~930 K. A temperature difference of approximately  $5^\circ \text{C}$  was applied between the two terminals of the sample in order to measure the Seebeck coefficient, whereas the electrical conductivity was measured using the four-probe method. The measurement uncertainties are 6% for both the electrical conductivity and Seebeck coefficient. The thermal conductivities ( $\kappa$ ) at RT~930 K were calculated as the product of the material densities, specific heats and thermal diffusivities (with uncertainty below 10%), which was measured using TC-1200RH. The heat capacities ( $C_p$ ) were estimated using Dulong–Petit rule,  $C_p = 3nR$  (where  $n$  is the number of atoms per formula unit,  $R$  is the gas constant). The total uncertainty for  $ZT$  is ~18%. The lattice contributions ( $\kappa_L$ ) were obtained by subtracting the electronic part ( $\kappa_e$ ) from the total  $\kappa$ , i.e.,  $\kappa_L = \kappa - \kappa_e$ . Here  $\kappa_e$  is expressed by the Wiedemann–Franz law,  $\kappa_e = L_0\sigma T$ , where  $L_0$  is the Lorenz number, estimated at  $1.5 \times 10^{-8} \text{ W}\Omega\text{K}^{-2}$  for not fully degenerate environment of semiconductors<sup>12</sup>.

The parameters were finalized after several repeated measurements using different samples.

## Results and Discussion

**Structural analyses.** The x-ray diffraction patterns (Fig. S1) shows that the materials can be indexed as a tetragonal cell<sup>20</sup> (PDF:51-1221) with  $a = 5.7461 \sim 5.7709$  and  $c = 11.4996 \sim 11.5340 \text{ \AA}$ , without any impurity phases identified in all the composition range ( $x = 0 \sim 0.5$ ). In XRD patterns several diffraction peaks are apparent, namely: (110), (202) or (210) and (114), which are characteristic of the CuIn<sub>3</sub>Se<sub>5</sub> phase with the space group  $I\bar{4}2m$ <sup>20,32–35</sup>. The lattice parameters  $a$  and  $c$ , which are in agreement with those reported<sup>24,25,35</sup>, both increase linearly with Te content increasing, see Fig. 1a. indicating that the chalcopyrite lattice suffers dilation upon Te substitution for Se. Since the tetragonal deformation parameter  $\eta$  and  $u$  are also directly related to the mean cation-anion distances  $d_{\text{I-VI}}$  and  $d_{\text{III-VI}}$  in chalcopyrite compounds<sup>31</sup>, an equal  $d_{\text{I-VI}}$  and  $d_{\text{III-VI}}$  values can be obtained as  $\eta$  (or  $u$ ) approaches unity (or 0.25)<sup>31</sup>. The calculated  $\Delta u$ ,  $d_{\text{Cu-Te}}$  and  $d_{\text{In-Te}}$  values are presented in



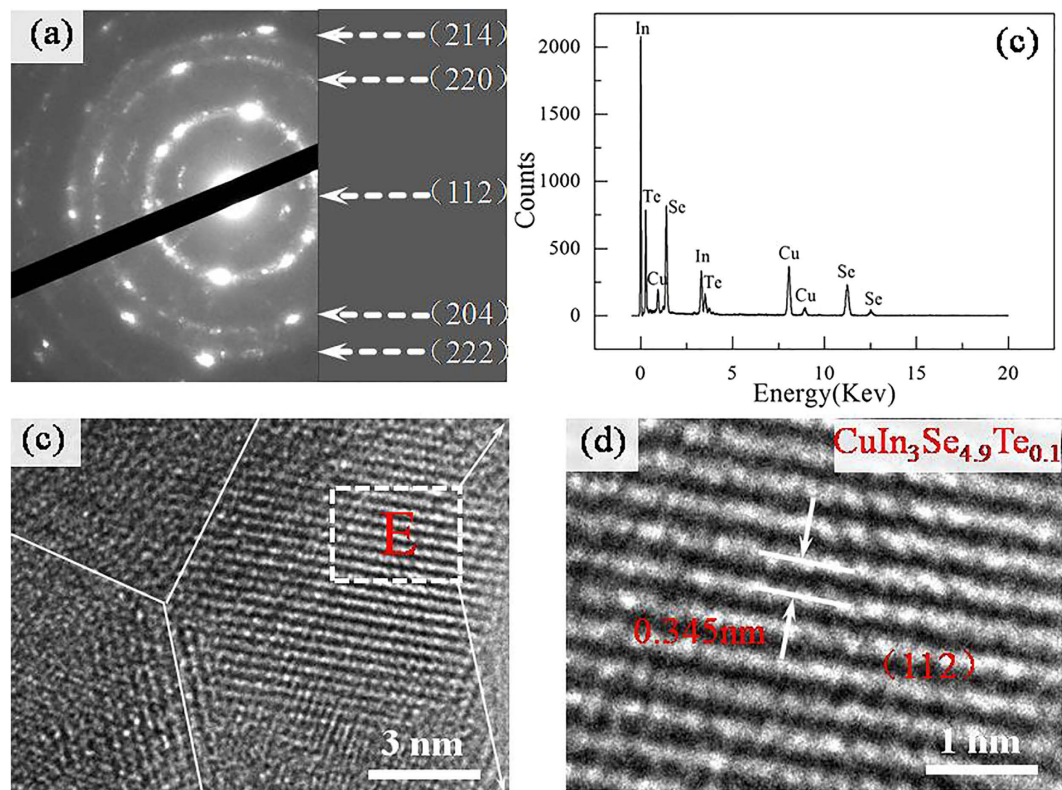
**Figure 1.** (a) Lattice constants  $a$  and  $c$  as a function of Te content ( $x$  value) in  $\text{CuIn}_3\text{Se}_{5-x}\text{Te}_x$ , they all increase linearly with  $x$  value; (b) Anion position displacement  $\Delta u = 0.25 - u$ , which decreases with  $x$  value. At  $x = 0.1$ ,  $\Delta u = 0.15 \times 10^{-3}$ , while at  $x \approx 0.15$ ,  $\Delta u = 0$ ; (c) Mean cation-Se distance  $d_{\text{Cu-Se}}$  and  $d_{\text{In-Se}}$  as a function of Te content ( $x$  value), at  $x \approx 0.15$ , i.e.  $\Delta u = 0$ , the difference between  $d_{\text{Cu-Se}}$  and  $d_{\text{In-Se}}$  gets the minimum.

Fig. 1b,c. With the Te content increasing, the  $\Delta u$  decreases gradually from  $0.32 \times 10^{-3}$  to  $-0.34 \times 10^{-3}$ , and it approaches zero at  $x \approx 0.15$  (Fig. 1b), at which  $d_{\text{Cu-Se}}$  roughly equals to  $d_{\text{In-Se}}$  (Fig. 1c).

In order to confirm the dilation of the crystal structure upon Te substitution, the microstructure analysis using HRTEM for the sample with  $x = 0.1$  is shown in Fig. 2, while that for Te-free sample is shown in Fig. S2 for comparison. Figure 2a is the selected area electron diffraction (SAED) pattern, and Fig. 2b,c are the EDS measurement results and high resolution image respectively. It is apparent that the materials show a conventional polycrystalline structure consisting of many nano-domains. The boundaries between nano-domains are not coherent, and ambiguously terminate at a grown domain 15~20 nm in size. Fig. 2d is the magnified high resolution TEM image, which shows that the  $d$  spacing between (112) crystal planes is about 0.345 nm. Figure S2a is SAED pattern, and Fig. S2b,c are the EDS measurement results and high resolution image for Te-free sample. Figure S2d is the magnified high resolution TEM image, which shows that the  $d$  spacing between (112) crystal plane is about 0.335 nm. An increase in  $d$  spacing upon Te substitution is resulted from the dilation of the crystal lattice, and is in accordance with the elongated lattice constants from XRD analyses.

**Transport properties and TE performance.** Although the isoelectronic substitution of Te for Se creates no extra electrons or holes, the dilation of the crystal structure upon such a substitution should have a profound impact on the structural and transport properties. In order to verify this conclusion, the Hall coefficients were measured at room temperature (RT), and the Hall carrier concentrations ( $n_{\text{H}}$ ) and mobility ( $\mu$ ) were then calculated. The results are shown in Fig. 3. The measured  $n_{\text{H}}$  value, which is  $4.11 \times 10^{21} \text{ m}^{-3}$  at  $x = 0$ , comparable to those from Jacob ( $3.40 \times 10^{21} \text{ m}^{-3}$ )<sup>36</sup> and Ariswan ( $1.16 \times 10^{21} \text{ m}^{-3}$ )<sup>37</sup>, reaches the highest ( $6.27 \times 10^{23} \text{ m}^{-3}$ ) at  $x = 0.1$  and then reduces to  $1.58 \times 10^{21} \text{ m}^{-3}$  at  $x = 0.5$ . While the mobility ( $\mu$ ) tends to increase from  $1.62 \text{ cm}^2 \text{ V}^{-1} \text{ s}^{-1}$ , which is less than that from Jacob ( $12.8 \text{ cm}^2 \text{ V}^{-1} \text{ s}^{-1}$ )<sup>36</sup>, to the highest  $35.48 \text{ cm}^2 \text{ V}^{-1} \text{ s}^{-1}$  at  $x = 0.5$ .

Since the carrier concentration is inversely related to the Seebeck coefficient ( $\alpha$ ), it is believed that there is a specific Te content at which the maximum  $\alpha$  value can be attained. Surprisingly, in the present work the sample at  $x = 0.1$  has the highest Seebeck coefficients among all samples below ~825 K (Fig. 4a), although the  $\alpha$  values



**Figure 2.** High resolution transmission electron microscopy (HRTEM) image observed in  $\text{CuIn}_3\text{Se}_{4.9}\text{Te}_{0.1}$ , (a) The selected area electron diffraction (SAED) pattern; (b) Chemical compositions analyses using EDS spectra; (c) High resolution TEM image, showing a conventional polycrystalline structure consisting of many nano-domains; (d) Magnified high resolution TEM image, which shows that the spacing between (112) crystal planes is about 0.345 nm.

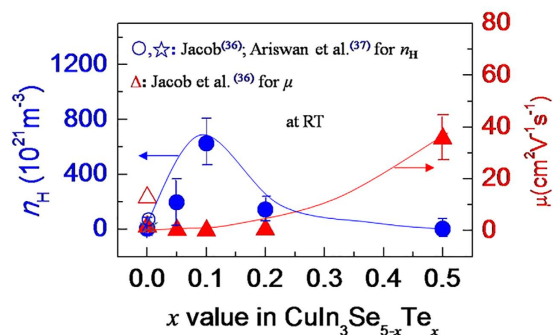


**Figure 3.** Measured Hall carrier concentration ( $n_H$ ) and mobility ( $\mu$ ) against  $x$  value in  $\text{CuIn}_3\text{Se}_{5-x}\text{Te}_x$ . The results from Jacob<sup>36</sup>, Ariswan *et al.*<sup>37</sup> are presented for comparison.

for different samples converge at high temperatures. The sample at  $x=0.1$  gives the highest  $\sigma$  value at  $\sim 930$  K, at which the  $\alpha$  and  $\sigma$  values are  $-292.58 \mu\text{V.K}^{-1}$  and  $2.05 \times 10^3 \Omega^{-1} \text{ m}^{-1}$  respectively (Fig. 4b). The lattice contribution  $\kappa_L$  as a function of temperature is shown in Fig. 4c, where the  $\kappa_L$  value reduces with temperature increasing for all the samples. The  $\kappa_L$  value at  $x=0.1$  is the lowest over the entire temperature range, and at  $T=930$  K it gives  $0.37 \text{ WK}^{-1} \text{ m}^{-1}$ . At  $x \geq 0.1$  the  $\kappa_L$  increases with  $\kappa_L = 0.61 \text{ WK}^{-1} \text{ m}^{-1}$  ( $x=0.2$ ) and  $0.52 \text{ WK}^{-1} \text{ m}^{-1}$  ( $x=0.5$ ). An insert is the total thermal conductivity  $\kappa$ , which has a similar composition dependence with  $\kappa_L$ , suggesting the heat carrying by phonons dominates in these compounds.

Combining the three physical parameters ( $\alpha$ ,  $\sigma$  and  $\kappa$ ), the dimensionless figure of merit (ZT) is shown in Fig. 4d. The highest ZT value of the sample at  $x=0.1$  is 0.4 at 930 K. An insert is the plot of ZT against  $x$  value in  $\text{CuIn}_3\text{Se}_{5-x}\text{Te}_x$ . Although this ZT value is still lower than those of other chalcopyrites, such as  $\text{CuGaTe}_2$ -based ( $ZT = 1.22$  at  $850 \text{ K}^{13}$ ;  $0.91 \sim 1.07$  at  $703 \text{ K}^{17,19,38}$ ;  $1.4$  at  $940 \text{ K}^{39}$ ),  $\text{AgInSe}_2$ -based alloys ( $1.05$  at  $815 \text{ K}^{18}$ , and  $\text{CuInTe}_2$ -based ( $0.69$  at  $737 \text{ K}^{40}$ ,  $1.18$  and  $1.3$  at  $850 \text{ K}^{41,42}$ ), it is  $\sim 2.6$  times that of intrinsic  $\text{CuIn}_3\text{Se}_5$  ( $ZT = \sim 0.15$ ).

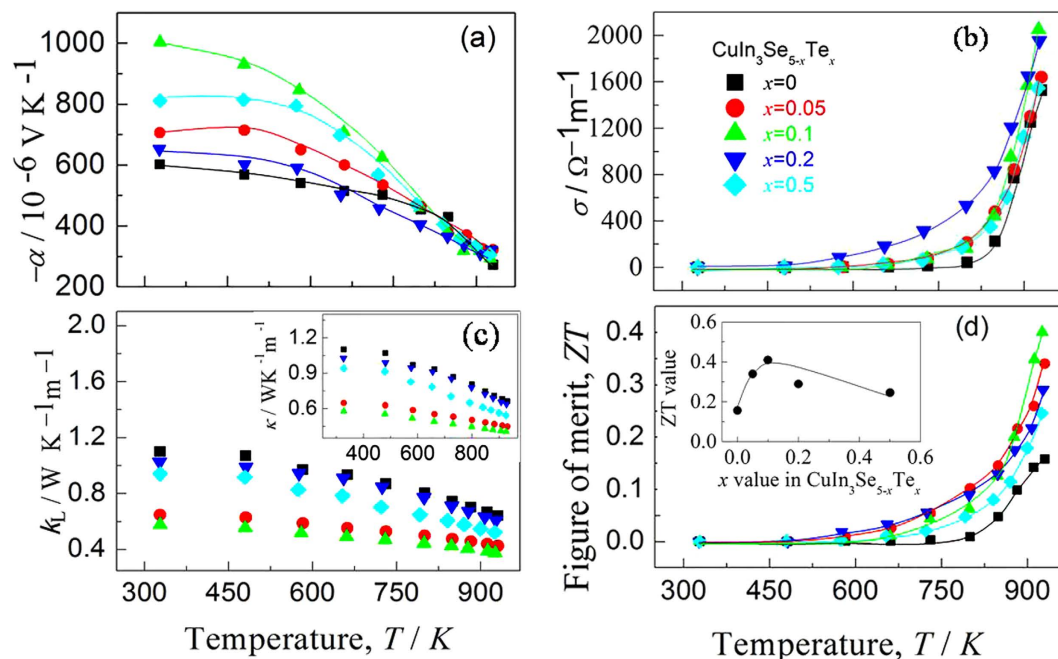
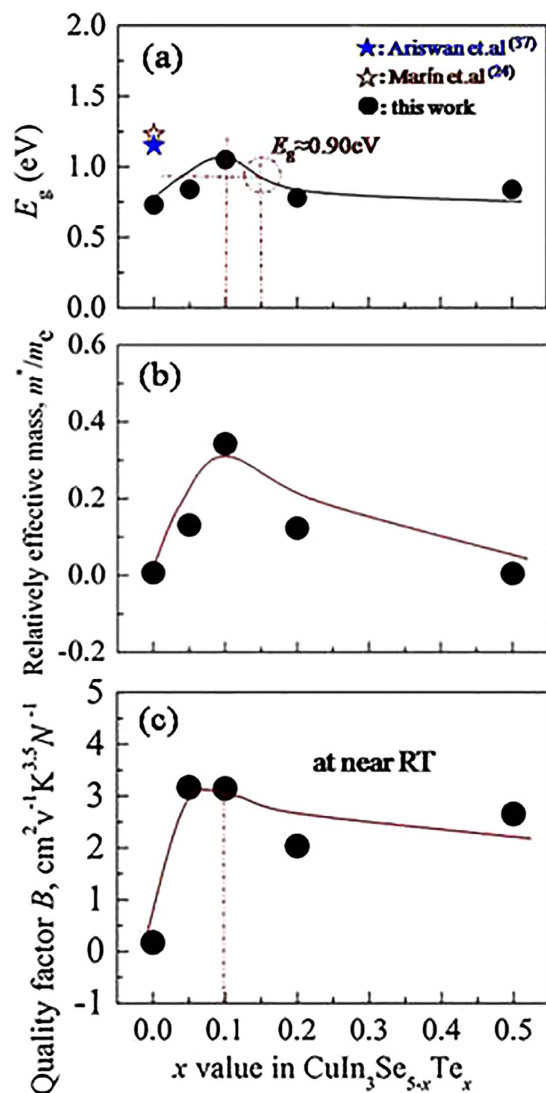


**Figure 4.** TE properties as function of temperature, (a) Seebeck coefficient ( $\alpha$ ); (b) Electrical conductivity ( $\sigma$ ); (c) lattice thermal conductivity ( $\kappa_L$ ), where an inset is the total  $\kappa$ ; (d) ZT values, an inset is the relation of ZT value with Te content ( $x$  value).

Upon the substitution of element Te for Se, we engineer the crystal structure (Fig. 1). At  $x = 0.1$ , there is a relatively big difference between  $d_{\text{Cu-Se}}$  and  $d_{\text{In-Se}}$ , along with the highest carrier concentration. Therefore, the lowest  $\kappa_L$  values are mainly due to the heavy phonon scattering caused by the lattice distortion, coupled with the phonon-carrier interaction. However, the phonon-carrier scattering strength is relatively less important in the temperature range of the present study, therefore, the phonon scattering in the lattice defects plays a major role in reducing the  $\kappa_L$  value. Furthermore, both the Seebeck coefficient and carrier concentration reach the highest at  $x = 0.1$  simultaneously, which is not consistent with the common relationship between the Seebeck coefficient and carrier concentration. We believe that the origin might be due to the alteration of the band structure.

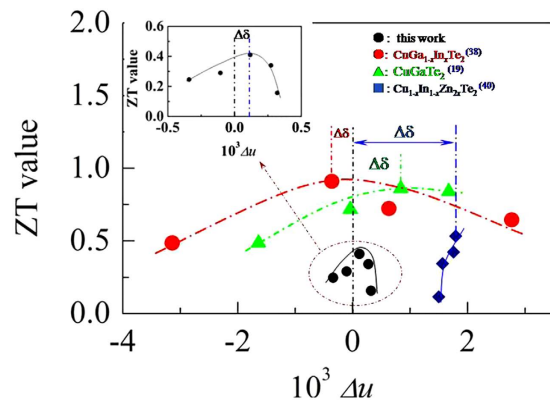
In order to gain a deep understanding of the band structure upon Te incorporation, the Pisarenko plots are shown in Fig. S3, assuming  $m^* = 0.006, 0.08, 0.11$  and  $0.34m_e$  at RT respectively. The data from Jacob<sup>36</sup> and Dejille *et al.*<sup>27</sup> are plotted together for comparison. The  $\alpha$  values for the Te-incorporated samples at RT slightly increase with  $n_H$  increasing, but the Pisarenko relations can exactly capture the measured values of Seebeck coefficient under assumed effective masses  $m^*$ . In this sense, the alteration of the bandgap should be taken into consideration.

Figure 1c shows the simultaneous elongation of the bond lengths  $d_{\text{Cu-Se}}$  and  $d_{\text{In-Se}}$ . This elongation is mainly caused by the increased repulsion between cation and anion upon Te substitution for Se, due to the lower electronegativity of Te (2.1) than that of Se (2.5), thus increasing the covalency degree<sup>43</sup>. In fact, the bond length  $d_{\text{Cu-Se}}$  increases more rapidly than  $d_{\text{In-Se}}$  with Te content increasing. As consequence, when  $x$  exceeds  $\sim 0.15$  the bond length  $d_{\text{Cu-Se}}$  is longer than  $d_{\text{In-Se}}$ . This suggests that the hybridization (bonding) between Cu- $d$  and Se- $p$  near the bandgap region has been weakened, resulting in the increased bandgap energy<sup>44-46</sup>. To confirm this result, the bandgap ( $E_g$ ) is estimated as a function of  $x$  value using  $E_g = 2\alpha_{\text{max}}eT^{47}$ , here  $T$  is the temperature at which  $\alpha$  appears with the maximum value. Although such an estimation could result in a large deviation of  $E_g$ <sup>48</sup>, it can roughly estimate the variation tendency of the  $E_g$  value with chemical composition in some chalcopyrites, for example, the variation tendency of the  $E_g$  value with Mn content in Mn-incorporated  $\text{Cu}_3\text{Ga}_5\text{Te}_9$  system<sup>49</sup>. The results are shown in Fig. 5a. The  $E_g$  values obtained in this work are still less than reported by Ariswan (1.15 eV)<sup>37</sup> and Marin (1.23 eV)<sup>24</sup>. However, it is observed that the bandgap ( $E_g$ ) is rapidly enlarged with Te content increasing, and at  $x = 0.1$  ( $\Delta u = 0.15 \times 10^{-3}$ ) it reaches the highest value of 1.05 eV. Above  $x = 0.1$  it is gradually reduced with Te content increasing. At  $x \approx 0.15$  ( $\Delta u = 0$ ) the  $E_g$  value is estimated to be  $\sim 0.90$  eV. The reduction in  $E_g$  above  $x \geq 0.1$  might be due to the reduced ionicity upon Te substitution for Se, proposed by Honeyman after he observed that energy gap increases with the crystalline ionicity increasing<sup>50</sup>. Since the high energy gap could prevent the degradation of thermoelectric power through inhibiting the formation of the thermally activated minority carriers<sup>6,51</sup>, that is why we have observed the highest Seebeck coefficients (Fig. 4a) and carrier concentration (Fig. 3) at  $x = 0.1$ . In addition, upon the substitution of Te for Se the relatively effective mass of the carrier ( $m^*/m_e$ ) increases rapidly with Te content from  $m^*/m_e = 0.007$  ( $x = 0$ ) to  $m^*/m_e = 0.342$  ( $x = 0.1$ ) ( $m_e$ : mass of the electron), and then decreases with Te content increasing at  $x \geq 0.1$ , see Fig. 5b, which suggests that a proper substitution of Te could optimize the band structures.



**Figure 5.** (a)  $E_g$  value, roughly estimated using  $E_g = 2\alpha_{\text{max}}eT$ , against  $x$  value, which increases with  $x$  value increasing until at  $x=0.1$ . At  $x \approx 0.15$   $E_g \approx 0.90$  eV. The  $E_g$  values from Ariswan<sup>37</sup> and Marín *et al.*<sup>24</sup> are presented for comparison.; (b) The relatively effective mass ( $m^*/m_e$ ) as a function of Te content. At  $x=0.1$  the highest  $m^*/m_e$  value is obtained; (c) The quality factor  $B$  at RT, defined by  $B = \mu_{\text{H}}(m^*/m_e)^{3/2}T^{5/2}/\kappa_{\text{L}}$ , as a function of  $x$  value. The  $B$  value increases until at  $x=0.1$ , and then decreases with  $x$  increasing.

Since the chalcopyrite compound at  $x=0.1$  has the highest  $m^*/m_e$  value, carrier concentration and lowest  $\kappa_{\text{L}}$  value, hence a highest quality factor  $B$  ( $B = \mu_{\text{H}}(m^*/m_e)^{3/2}T^{5/2}/\kappa_{\text{L}}$ )<sup>12</sup> can be anticipated. We therefore plot  $B$  value at near RT as a function of  $x$ , shown in Fig. 5c. In Fig. 5c we observed that the  $B$  value rapidly increases with  $x$  value increasing until  $x=0.1$ , and then it decreases. Therefore, we consider that it is not necessary to let  $x > 0.1$  ( $\Delta u = 0.15 \times 10^{-3}$  at  $x=0.1$ ) in order to improve the TE performance. When  $x > 0.1$  (for example:  $\Delta u \rightarrow 0$  when  $x \rightarrow 0.15$ ), the TE performance may degrade owing to the enhanced lattice contribution  $\kappa_{\text{L}}$ . In fact, the ZT value reaches the highest at  $x=0.1$  (see the insert in Fig. 4d), corresponding to  $\Delta u = 0.15 \times 10^{-3}$ . ZT value vs  $\Delta u$  is plotted in Fig. 6, where the ZTs against  $\Delta u$  in other chalcopyrite compounds, such as,  $\text{CuGa}_{1-x}\text{In}_x\text{Te}_2$ <sup>38</sup>, annealed  $\text{CuGaTe}_2$ <sup>19</sup> and  $\text{CuIn}_{1-x}\text{Zn}_x\text{Te}_2$ <sup>40</sup>, are also presented for comparison. It is worth noting that at  $\Delta u=0$ , corresponding to  $x=0.15$ , neither the  $E_g$  ( $E_g \approx 0.90$  eV) nor the ZT value reaches the highest, see Figs 5a and 6. The insert in Fig. 6 is close-up view of present relation between ZTs and  $\Delta u$  in this work. These chalcopyrite compounds all show that they do not have the highest ZTs at  $\Delta u=0$ , but at a certain  $\Delta u$  value, i.e. at a distance ( $\Delta\delta$ ) from  $\Delta u=0$  they give the highest ZTs. This indicates that the best TE performance can be achieved with a certain crystal structure parameters for each chalcopyrite compound with a specific space group. This finding is in good agreement with the previous assumption that when  $\Delta u=0$  or  $\eta=1$  it is difficult to achieve the highest TE performance for some chalcopyrite compounds, due not only to electrical inactivity, but also a relatively high lattice part  $\kappa_{\text{L}}$ .



**Figure 6. The ZTs against  $\Delta u$ .** The maximum ZTs from different chalcopyrites, such as,  $\text{CuGa}_{1-x}\text{In}_x\text{Te}_2$ <sup>38</sup>, annealed  $\text{CuGaTe}_2$ <sup>19</sup> and  $\text{Cu}_{1-x}\text{In}_{1-x}\text{Zn}_{2x}\text{Te}_2$ <sup>40</sup> are presented for comparison. These chalcopyrite compounds all show that they do not have the highest ZTs at  $\Delta u = 0$ , but at a certain  $\Delta u$  value. An insert is close-up view of present relation between ZTs and  $\Delta u$ . The ZT value reaches the highest at  $\Delta u = 0.15 \times 10^{-3}$ , rather than at  $\Delta u = 0$ .

## Conclusions

In this work the chalcopyrite compounds  $\text{CuIn}_3\text{Se}_{5-x}\text{Te}_x$  ( $x = 0 \sim 0.5$ ) with space group  $I\bar{4}2m$  have been prepared, and the dilation of the crystal structure as  $x$  value increases has been observed. At  $x = 0.15$  the anion position displacement  $\Delta u$  is tending to be zero. But at  $x = 0.1$  ( $\Delta u = 0.15 \times 10^{-3}$ ) both the band energy ( $E_g$ ) and the Hall carrier concentration  $n_H$  reach the highest values, leading to the best thermoelectric performance with the ZT value of 0.4 at 930 K. Furthermore, at  $x = 0.1$  it is the critical Te content in  $\text{CuIn}_3\text{Se}_{5-x}\text{Te}_x$  ( $x = 0 \sim 0.5$ ), above which the quality factor  $B$  decreases, and lattice thermal conductivity  $\kappa_L$  are higher than those at  $x = 0.1$ , caused by reduced phonon scattering in lattice defects. We therefore conclude that the best thermoelectric performance can be achieved at a certain  $\Delta u$  value ( $\Delta u \neq 0$ ) if one can engineer the crystal structures of the chalcopyrite with a specific space group.

## References

- Hochbaum, A. I. *et al.* Enhanced thermoelectric performance of rough silicon nanowires. *Nature* **451**, 163–167 (2008).
- Boukai, A. I. *et al.* Silicon nanowires as efficient thermoelectric materials. *Nature* **451**, 168–171 (2008).
- Poudel, B. *et al.* High-thermoelectric performance of nanostructured bismuth antimony telluride bulk alloys. *Science* **320**, 634–638 (2008).
- Pei, Y. *et al.* Convergence of electronic bands for high performance bulk thermoelectrics. *Nature* **473**, 66–69 (2011).
- Heremans, J. P. *et al.* Enhancement of thermoelectric efficiency in PbTe by distortion of the electronic density of states. *Science* **321**, 554–557 (2008).
- Pei, Y. *et al.* Band engineering of thermoelectric materials. *Adv. Mater.* **24**, 6125–6135 (2012).
- Zhao, L. *et al.* Ultrahigh power factor and thermoelectric performance in hole-doped single-crystal SnSe. *Science* **351**, 141–144 (2016).
- Zhao, L. *et al.* Ultralow thermal conductivity and high thermoelectric figure of merit in SnSe crystals. *Nature* **508**, 373–389 (2014).
- Liu, W. *et al.* Convergence of conduction bands as a means of enhancing thermoelectric performance of n-Type  $\text{Mg}_2\text{Si}_{1-x}\text{Sn}_x$  solid solutions. *Phys. Rev. Lett.* **108**, 166601 (2012).
- Liu, X. *et al.* Low Electron scattering potentials in high performance  $\text{Mg}_2\text{Si}_{0.45}\text{Sn}_{0.55}$  based thermoelectric solid solutions with band convergence. *Adv. Energy Mater.* **3**, 1238–1244 (2013).
- Yu, C. *et al.* High-performance half-Heusler thermoelectric materials  $\text{Hf}_{1-x}\text{Zr}_x\text{NiSn}_{1-y}\text{Sb}_y$ , prepared by levitation melting and spark plasma sintering. *Acta Mater.* **57**, 2757–2764 (2009).
- Shi, X. *et al.* Recent advances in high-performance bulk thermoelectric materials. *Inter. Mater. Rev.* **61**, 379–415 (2016).
- Zhang, J. *et al.* High-performance pseudocubic thermoelectric materials from non-cubic chalcopyrite compounds. *Adv. Mater.* **26**, 3848–3853 (2014).
- Zhang, S. B. *et al.* Stabilization of ternary compounds via ordered arrays of defect pairs. *Phys. Rev. Lett.* **78**, 4059–4062 (1997).
- Rincón, C. *et al.* Scattering of the charge carriers by ordered arrays of defect pairs in ternary chalcopyrite semiconductors. *Appl. Phys. Lett.* **80**, 998–1000 (2002).
- Wei, S. H. *et al.* Effects of Ga addition to  $\text{CuInSe}_2$  on its electronic, structural, and defect properties. *Appl. Phys. Lett.* **72**, 3199–3201 (1998).
- Cui, J. *et al.* Promising defect thermoelectric semiconductors of  $\text{Cu}_{1-x}\text{GaSb}_x\text{Te}_2$  ( $x = 0 \sim 0.1$ ) with the chalcopyrite structure. *J. Mater. Chem. A* **1**, 677–683 (2013).
- Wang, L. *et al.* Site Occupations of Zn in  $\text{AgInSe}_2$ -based chalcopyrites responsible for modified structures and significantly improved thermoelectric performance. *RSC Adv.* **4**, 33897–33904 (2014).
- Wu, W. C. *et al.* Manipulation of the crystal structure defects: An alternative route to the reduction in lattice thermal conductivity and improvement in thermoelectric performance of  $\text{CuGaTe}_2$ . *Appl. Phys. Lett.* **103**, 011905 (2013).
- Hanada, T. *et al.* Crystal structure of  $\text{CuIn}_3\text{Se}_5$  semiconductor studied using electron and X-ray diffractions. *Jpn. J. Appl. Phys.* **36**, L1494–L1497 (1997).
- Xiao, H. Z. *et al.* Structural, optical, and electrical properties of epitaxial chalcopyrite  $\text{CuIn}_3\text{Se}_5$  films. *J. Appl. Phys.* **76**, 1503–1510 (1994).
- Hernández, E. *et al.* Electrical properties of  $\text{CuIn}_3\text{Se}_5$  bulk crystal at low temperature. *Cryst. Res. Technol.* **37**, 1088–1093 (2002).
- Chang, C. *et al.* Local structure of  $\text{CuIn}_3\text{Se}_5$ : X-ray absorption fine structure study and first-principles calculations. *Phys. Rev. B* **68**, 054108 (2003).
- Marín, G. *et al.* X-ray powder diffraction and optical characterization of the  $\text{Cu}(\text{In}_{1-x}\text{Ga}_x)_3\text{Se}_5$  semiconducting system. *Mater. Res. Bull.* **33**, 1057–1068 (1998).

25. Philip, R. R. & Pradeep, B. Nonideal anion displacement, band gap variation, and valence band splitting in Cu-In-Se compounds. *Thin Solid Films* **472**, 136–143 (2005).
26. Diaz, R. & Arranz, A. Effect of the composition on the ionic motion in an In-rich chalcopyrite ingot of the Cu-Ag-In-Se system. *J. Alloys Compds.* **590**, 80–86 (2014).
27. Djellal, L. *et al.* Physical, photoelectrochemical properties of  $\text{CuIn}_3\text{Se}_5$  and relevance for hydrogen production. *Mater. Chem. Phys.* **137**, 340–345 (2012).
28. Paszkowicz, W. *et al.* Rietveld refinement for  $\text{CuInSe}_2$  and  $\text{CuIn}_3\text{Se}_5$ . *J. Alloys Compds.* **362**, 241–247 (2004).
29. Abrahams, S. C. & Bernstein, J. L. Piezoelectric Nonlinear Optic  $\text{CuGaS}_2$  and  $\text{CuInS}_2$  Crystal Structure: Sublattice Distortion in  $\text{A}^{\text{III}}\text{B}^{\text{VI}}$  and  $\text{A}^{\text{II}}\text{B}^{\text{IV}}\text{C}_2^{\text{V}}$  Type Chalcopyrites. *J. Chem. Phys.* **59**, 5415–5422 (1973).
30. Abrahams, S. C. & Bernstein, J. L. Piezoelectric Nonlinear Optic  $\text{CuGaSe}_2$  and  $\text{CdGeAs}_2$ : Crystal Structure, Chalcopyrite Microhardness, and Sublattice Distortion. *J. Chem. Phys.* **61**, 1140–1146 (1974).
31. Jaffe, J. E. & Zunger, A. Electronic structure of the ternary chalcopyrite semiconductors  $\text{CuAlS}_2$ ,  $\text{CuGaS}_2$ ,  $\text{CuInS}_2$ ,  $\text{CuAlSe}_2$ ,  $\text{CuGaSe}_2$ , and  $\text{CuInSe}_2$ . *Phys. Rev. B* **28**, 5822–5847 (1983).
32. Yao, J. *et al.* Site preference of manganese on the copper site in Mn-Substituted  $\text{CuInSe}_2$  chalcopyrites Revealed by a combined neutron and x-ray powder diffraction study. *Chem. Mater.* **22**, 1647–1655 (2010).
33. Boehnke, U. C. & Kühn G. Phase relations in the ternary system Cu-In-Se. *J. Mater. Sci.* **22**, 1635–1641 (1987).
34. Yao, J. *et al.* Effects of Mn substitution on the structure and properties of chalcopyrite-type  $\text{CuInSe}_2$ . *J. Solid State Chem.* **182**, 2579–2586 (2009).
35. Wang, H. P. *et al.* Studies on monocrystalline  $\text{CuInSe}_2$  and  $\text{CuIn}_3\text{Se}_5$ . *Thin Solid Films* **361–362**, 494–497 (2000).
36. Jacob, R. *et al.* Optoelectronic and low temperature thermoelectric effects in the OVC n- $\text{CuIn}_3\text{Se}_5$  thin films. *Phys. Sta. Sol. A* **209**, 2195–2200 (2012).
37. Ariswan *et al.* Structural, optical and electrical properties of the ordered vacancy compound  $\text{CuIn}_3\text{Se}_5$  thin films fabricated by flash evaporation. *Solid State Commun.* **124**, 391–396 (2002).
38. Li, Y. *et al.* High thermoelectric performance of solid solutions  $\text{CuGa}_{1-x}\text{In}_x\text{Te}_2$  ( $x=0-1.0$ ). *Appl. Phys. Lett.* **100**, 231903 (2012).
39. Plirdpring, T. *et al.* Chalcopyrite  $\text{CuGaTe}_2$ : A high-efficiency bulk thermoelectric material. *Adv. Mater.* **24**, 3622–3626 (2012).
40. Yang, J. *et al.* Lattice defects and thermoelectric properties: the case of p-type  $\text{CuInTe}_2$  chalcopyrite on Introduction of Zinc. *Dalton Trans.* **43**, 15228–15235 (2014).
41. Liu, R. *et al.* Ternary compound  $\text{CuInTe}_2$ : a promising thermoelectric material with diamond-like structure. *Chem. Commun.* **48**, 3818–3820 (2012).
42. Carr, Winston D. & Morelli, Donald T. Influence of doping and solid solution formation on the thermoelectric properties of chalcopyrite semiconductors. *J. Alloys Compds.* **630**, 277–281 (2015).
43. Ma, C. G. & Brik, M. G. First principles studies of the structural, electronic and optical properties of  $\text{LiInSe}_2$  and  $\text{LiInTe}_2$  chalcopyrite crystals. *Solid State Commun.* **203**, 69–74 (2015).
44. Ozaki, S. & Adachi, S. Optical absorption and photoluminescence in the ternary chalcopyrite semiconductor  $\text{AgInSe}_2$ . *J. Appl. Phys.* **100**, 113526 (2006).
45. Shay, J. L. *et al.* Electronic Structure of  $\text{AlInSe}_2$  and  $\text{CuInSe}_2$ . *Phys. Rev. B* **7**, 4485–4490 (1973).
46. Shay, J. L. & Kasper, H. M. Direct Observation of Cu *d* Levels in I-III-VI<sub>2</sub> Compounds. *Phys. Rev. Lett.* **29**, 1162–1164 (1972).
47. Goldsmid, H. J. & Sharp, J. W. Estimation of the thermal band gap of a semiconductor from Seebeck measurements. *J. Elect. Mater.* **28**, 869–872 (1999).
48. Gibbs, Z. M. *et al.* Band gap estimation from temperature dependent Seebeck measurement—deviations from the  $2e|S|_{\text{max}}T_{\text{max}}$  relation. *Appl. Phys. Lett.* **106**, 022112 (2015).
49. Cui, J. *et al.* Engineering the energy gap near the valence band edge in Mn-incorporated  $\text{Cu}_3\text{Ga}_5\text{Te}_9$  for an enhanced thermoelectric performance. *J. Mater. Chem. C*, **4**, 8014 (2016).
50. Honeyman, W. N. & Wilkinson, K. H. Growth and properties of single crystals of group I–III–VI<sub>2</sub> ternary semiconductors. *J. Phys. D: Appl. Phys.* **4**, 1182–1185 (1971).
51. Pei, Y. *et al.* Stabilizing the optimal carrier concentration for high thermoelectric efficiency. *Adv. Mater.* **23**, 5674–5678 (2011).

## Acknowledgements

This work is supported by the National Natural Science Foundation of China (51671109, 51171084), Zhejiang Provincial Natural Science Foundation (LY14E010003, LQ14E010001), and Natural Science Foundation of Ningbo (2015A610044).

## Author Contributions

Yufu Lu and Shaoping Chen prepared materials & samples and performed experiments on thermoelectric transport properties; Wenchang Wu and Zhengliang Du prepared the samples for high resolution TEM (HRTEM) and observed the microstructures; Jiaolin Cui and Yimin Chao designed the study and wrote the manuscript.

## Additional Information

**Supplementary information** accompanies this paper at <http://www.nature.com/srep>

**Competing financial interests:** The authors declare no competing financial interests.

**How to cite this article:** Lu, Y. *et al.* Enhanced thermoelectric performance of a chalcopyrite compound  $\text{CuIn}_3\text{Se}_{5-x}\text{Te}_x$  ( $x=0-0.5$ ) through crystal structure engineering. *Sci. Rep.* **7**, 40224; doi: 10.1038/srep40224 (2017).

**Publisher's note:** Springer Nature remains neutral with regard to jurisdictional claims in published maps and institutional affiliations.



This work is licensed under a Creative Commons Attribution 4.0 International License. The images or other third party material in this article are included in the article's Creative Commons license, unless indicated otherwise in the credit line; if the material is not included under the Creative Commons license, users will need to obtain permission from the license holder to reproduce the material. To view a copy of this license, visit <http://creativecommons.org/licenses/by/4.0/>

© The Author(s) 2017